

An Anti-Vibration Time Delay Integration CMOS Image Sensor with Online Deblurring Algorithm

Hang Yu, *Student Member, IEEE*, Xinyuan Qian, Menghan Guo,
Shoushun Chen, *Senior Member, IEEE*

Abstract—This paper presents an anti-vibration time delay integration (TDI) CMOS image sensor for small remote imaging systems, introducing a hardware-implemented online deblurring (ODB) algorithm to address the image blur problems caused by vibrations. The proposed sensor has 8 TDI stages, column-parallel TDI accumulating and online deblurring circuits. A 256×8 -pixel prototype chip was fabricated using a $0.18 \mu\text{m}$ CMOS image sensor technology with a pixel footprint of $6.5 \mu\text{m} \times 6.5 \mu\text{m}$ and a fill factor of 28%. Measurement results show that the sensor can achieve dynamic ranges of 45.1dB and 51.8dB, respectively, with and without enabling the ODB algorithm. Compared to a single-stage line scanner imager, it offers an improvement in signal-to-noise ratios of 1.9dB and 8.6dB, respectively, with and without the ODB algorithm.

Index Terms—CMOS image sensor, time delay integration, online deblurring algorithm, remote imaging system.

I. INTRODUCTION

Time delay integration (TDI) image sensors have a wide range of applications, including satellite imaging, military reconnaissance, document scanning and industrial conveyor belt inspection systems [1–8]. In a TDI image sensor, several stages of pixels are placed in the across-track direction, and the panoramic image in the along-track direction is thus acquired with the movement of the sensor. Unlike single-stage line scanners, TDI image sensors contain more than one stage of pixels, exposed to the same target many times in order to extend the optical integration time and significantly improve signal strength.

The operating principle of a TDI image sensor is illustrated in Fig. 1 [5]. For the sake of clarity, we take 4-stage TDI as example to explain the operation. 4 pixel stages are shown in one column in the along-track direction, t_1 , t_2 , t_3 and t_4 represent the respective TDI image sensor positions in sequential time. With the sensor focusing on object A on the ground, at t_1 A is projected at the first pixel in the column, producing photo signal A_1 . As the camera moves, another photo signal of A is generated at t_2 by the second pixel. A_2 is regarded as the sum of the photo signals acquired from the

first two pixels. At t_3 , the third pixel is marked in the same way as in the first two cases, creating the third photo signal and, accordingly, A_3 indicates the sum of the photo signals from the first three pixels. At t_4 , the fourth pixel produces another photo signal, and A_4 represents all the photo signals from the four pixels and the output as the final photo signal. Seen from the whole process, the photo signals collected from each pixel do not directly output after integration, but are shifted to the next stage of pixels in the same column, adding the previously acquired photo signals to the total. The final output signals are summed over a number of TDI stages available in this way. Apparently, a TDI image sensor with n pixel stages can extend the effective integration time by n times. For an integration mode camera, the final photo signal is increased by n times. In contrast, the dynamic range (DR) will be decreased by \sqrt{n} times due to input-referred noise and dark current, and the signal-to-noise ratio (SNR) is therefore increased by \sqrt{n} times [6, 9].

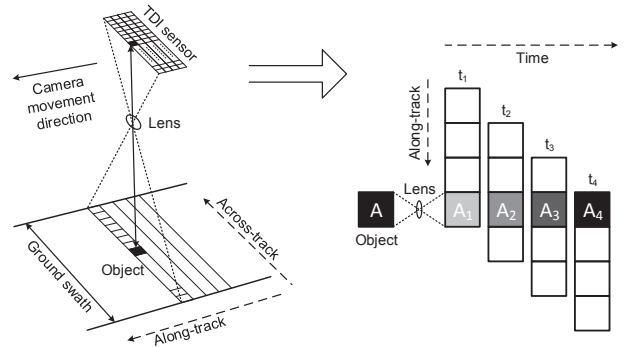


Fig. 1. TDI image sensor system.

Although CMOS technologies have now taken the biggest market share for consumer image sensors, CCDs still constitute the predominant technology of choice in TDI image sensors. Thanks to their innate charge transfer operation and high charge transfer efficiency, CCDs can easily carry out TDI operations without the need for any additional circuits [10–12]. In contrast, CMOS technology has more difficulties to overcome when performing TDI operations. Several single-chip-integrated TDI image sensor designs based on CMOS technology were recently published. The TDI architectures of these sensors can be mainly divided into two groups: adjacent pixel signal transfer and signal accumulator. Adjacent pixel signal transfer [5–7] is the method most similar to that employed in CCD TDI operation, and the basic idea

is to use a column-shared unity-gain buffer to transfer the photo signal voltage between neighbouring pixels in the along-track direction. Since the unity-gain buffer can be powered off during integration, this methodology could dramatically reduce power consumption. However, the complicated cross-pixel signal paths take up a large silicon area, which limit the total number of TDI stages that can be used; while the signal accumulator [2–4] functions like a multi-stage switched-capacitor integrator, with each stage containing a capacitor for signal accumulation. For more TDI stages, this methodology therefore needs more capacitors. Furthermore, the signal accumulator has to be turned on during the whole integration phase, so power consumption is high.

Due to their limited charge transfer modes, TDI-CCD and most TDI CMOS image sensors can only operate successfully under the assumptions that object movement relative to the sensor is synchronized with the traveling of the charge packets or photo signals on the focal plane, and that the direction of the object movement is perfectly crosswise to the rows of pixels. In industrial applications, in which the relative movement of the object to the sensor can be accurately controlled, high quality imaging can be guaranteed [8]. However in remote imaging systems such as satellites, flight stability is sometimes affected by vibrations caused by flexible internal components and/or by the external environment. Camera movement is no longer stable, so that conventional TDI schemes will produce blurred images.

In this paper, we present an online deblurring (ODB) algorithm implemented in an 8-stage TDI CMOS image sensor (CIS). The algorithm can compensate image shift on the focal plane, and produce a sharp image even in scenarios involving complicated vibrations. A prototype image sensor was fabricated using a $0.18\mu\text{m}$ CMOS image sensor process. The rest of the paper is organized as follows: Section II discusses the vibration problem and the idea of the proposed algorithm; Section III elaborates on the TDI image sensor design; Section IV analyzes the noise introduced by the TDI signal path; Section V describes the chip implementation and measurement results, and Section VI presents some conclusions.

II. PROBLEM STATEMENT AND ALGORITHMIC DESIGN

A. Problem Statement

Satellites in orbit are sometimes affected by random disturbances. According to the open data of the exiting satellites, such as LANDSAT-4 of NASA/GSFC [13] and OLYMPUS satellite of ESA [14], the random disturbances contain plenty of harmonic vibrations (sine wave), and their frequencies are concentrated below 500Hz. The main harmonic vibration is at around $1\sim 2.2\text{Hz}$ caused by solar panel tuning. The reaction wheel (momentum wheel) also contributes harmonic vibration at $100\sim 200\text{Hz}$ when changing the rotation speed. Another harmonic vibration is generated by motor and motorized pumps at hundreds Hz. Moreover, jet blast, pointing control, spacecraft orbital motion, attitude changes and the Earth's rotation error also have contributions to the disturbance [15, 16].

In a remote TDI imaging system, the aforementioned vibrations will introduce residual motion, referring to motion

in the across-track direction and excluding the along-track scanning motion, which leads to blurred and distorted images. In the literature, a number of works have been done to improve the image quality. Big satellites are often equipped with active vibration control, a means of attenuating unwanted on-board vibrations, as an alternative to passive absorbers [16–18]. However, small satellites usually do not have the luxury due to limited budget of volume, weight and power. For example, nano-satellites are miniature satellites that are typically weighing in the range of $1\sim 20\text{kg}$, and only have a total power in the range of $20\sim 50\text{Watt}$. More research efforts are found in the area of image post-processing. The popular methods mainly fall into two categories: non-blind deblurring [19–23] and blind deblurring [24–26]. The difference between them lies in the motion blur kernel or point spread function (PSF), which can be known or computed in non-blind cases, and unknown in blind cases. Non-blind deblurring usually has higher accuracy than blind cases because of noise and ring artifacts. However, non-blind cases need the assistant of extra imaging system and even complicated optical system with heavy weight and large volume, so that they are also not suitable for small remote imaging system.

B. Algorithm Consideration

For the sake of clarity, a 4-stage TDI is used here to explain the idea. As can be seen in Fig. 2, *A*, *B* and *C* are three objects placed close to each other on the ground, and each one is projected onto one pixel on the sensor's focal plane. Their brightness signals are used as a reference in the following stages. In an ideal TDI, the subsequent stages should always image the same sets of objects and accumulate their photo signals. Fig. 2(a) shows this scenario.

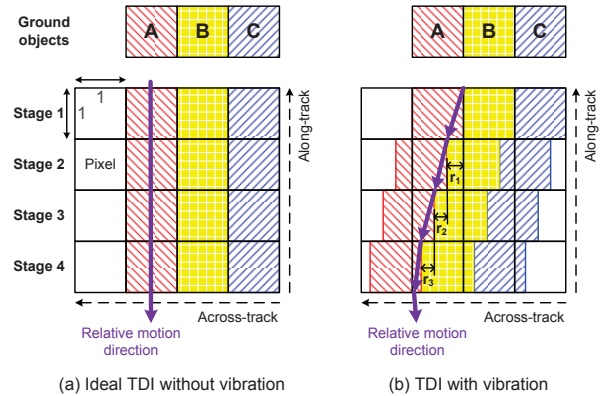


Fig. 2. TDI images with (b) and without (a) vibration on the focal plane.

However, when vibration occurs, the subsequent stages will have column-wise misalignment. One pixel could image two objects together, as shown in Fig. 2(b). Assuming the photo signal densities of each object on the focal plane after optical system are evenly distributed, since the integration time in each TDI stage is split equally, the photo signal can be directly calculated by photo signal density and pixel area. And assuming pixel size is one unit, the relative image shifts in the following TDI stages are r_1 , r_2 and r_3 , respectively. For

the second column, the photo signals captured from each TDI stage can be expressed as:

$$Y_{A1} = a \quad (1)$$

$$Y_{A2} = Y_{A1} + r_1(-a + b) \quad (2)$$

$$Y_{A3} = Y_{A2} + r_2(-a + b) \quad (3)$$

$$Y_{A4} = Y_{A3} + r_3(-a + b) \quad (4)$$

where b stands for the signal strength of object B , which is captured by the pixel in the first stage, third column. Under these circumstances, if conventional TDI protocol is followed and all the photo signals are summed unconditionally, the final photo signal is neither the pure signal from object A nor that from B , but rather a mixture of both, resulting in a blurred image.

The signal differences between each two neighbouring stages can be found from Eq. (1)~Eq. (4), and the total signal difference can be calculated as

$$\begin{aligned} \Delta Y &= 3 \times r_1(a - b) + 2 \times r_2(a - b) + 1 \times r_3(a - b) \\ &= 3(Y_{A1} - Y_{A2}) + 2(Y_{A2} - Y_{A3}) + (Y_{A3} - Y_{A4}) \end{aligned} \quad (5)$$

Note that ΔY is expressed as a weighted summation of the signal differences between each two neighbouring stages, implying a compensation algorithm. By accumulating the signal differences between each two neighbouring stages in the same column and associating them with appropriate gains, the desired “clean” signal can then be derived by conventional TDI accumulations and auxiliary stage-differential calculations. This method can be generalized to an n -stage TDI image sensor, the general expression of the “clean” signal being

$$Y = \sum_{i=1}^n Y_{Ai} + \sum_{i=1}^{n-1} (n - i) [Y_{Ai} - Y_{A(i+1)}] \quad (6)$$

This expression clearly suggests that the algorithm can be implemented by two sets of gain amplifiers (GA).

C. Simulation Results

A model of a TDI image sensor was built with Matlab, and used to compare the performance of a conventional TDI scheme with that of the ODB algorithm. Fig. 3 shows the simulation results for a map of black-white line pairs (an 8-bit monochrome image) with an 8-stage TDI model. The number of TDI stages selected was 8, taking into account the trade-off between SNR and DR [5]. The simulation followed the assumption that with that number of TDI stages, the output would be well integrated without being saturated. Since the same vibration amplitude could cause different image shifts on the focal plane with different optical systems, focal plane image shift was directly applied here as a metric of vibration level. Unidirectional and bidirectional vibration scenarios were simulated, each with a half-pixel shift per stage. It was clearly shown that the ODB algorithm is capable of generating a sharp output image while the conventional TDI produces a blurred one. To further quantify the performance, we applied an average sharpness function (ASF) that is widely

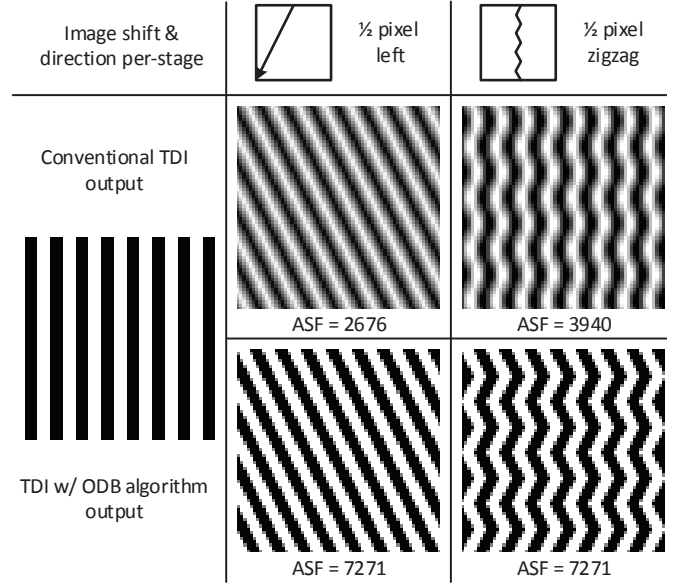


Fig. 3. Simulation results for a map of black-white line pairs. Column 1 is the original image, Column 2 and 3 represent the output images under unidirectional and bidirectional vibration scenarios respectively. For each vibration mode, two sets of output images produced by both conventional TDI scheme and the ODB algorithm are obtained.

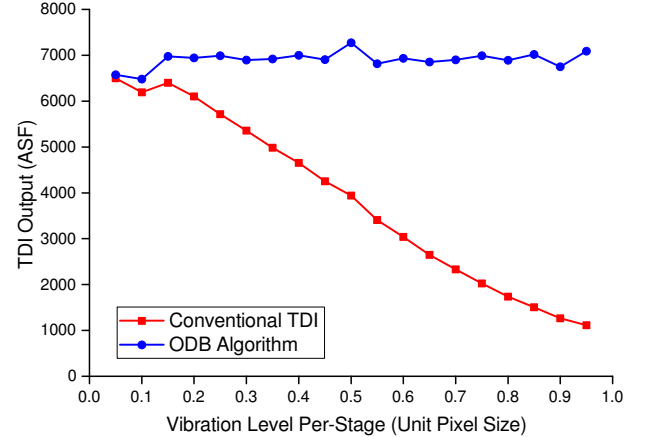


Fig. 4. TDI output comparison between conventional TDI scheme and the ODB algorithm with variable image shifts (number of TDI stages = 8).

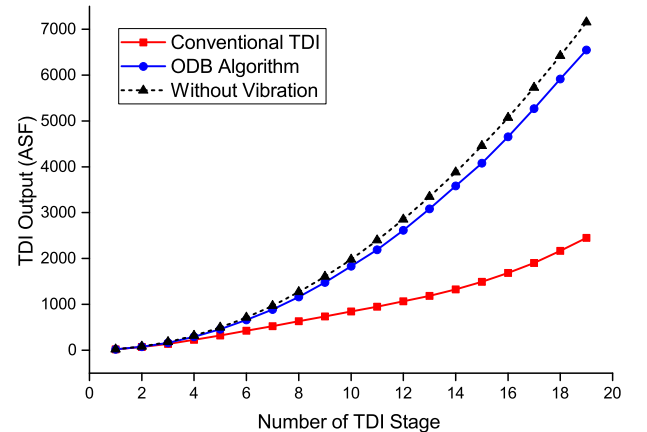


Fig. 5. TDI output comparison between conventional TDI scheme and the ODB algorithm with variable numbers of TDI stages.

used in auto-focus algorithms as a figure of merit [27]. The ASF is defined as the average squared-gradient over the whole image, and can be expressed as

$$ASF = \left(\sum_{j=1}^C \sum_{i=1}^R |y(i+1, j) - y(i, j)|^2 \right) / CR \quad (7)$$

where, $y(i, j)$ denotes the luminance or grey level of an image of size $R \times C$.

To further evaluate the efficiency of the ODB algorithm, we also simulated its performance with respect to variable image shifts per stage and different numbers of TDI stages. Fig. 4 shows the simulation results with vibration level as a variable (while the number of TDI stages is fixed as 8). It is clear that the conventional TDI scheme is very sensitive to vibration. The sharpness of the output images decreases with more image shift, or equivalently higher level of vibrations. To the contrast, the ODB algorithm can retain the output images with high ASF values, even at very high level of vibration. Fig. 5 shows the simulation results for the same input image with variable numbers of TDI stages. When the number of TDI stages is 1 (i.e., single row scanning imager), the performances of the two solutions are the same, making the ASF values of the outputs identical. As the number of TDI stages increases, the corresponding integration time also rises, as do the signal level of the outputs. Without vibration, the sharpness should increase in square with the number of TDI stages. The result clearly shows that the proposed ODB algorithm allows the sharpness grows much faster than the conventional TDI scheme. Moreover, the ODB algorithm requires no prior knowledge of the variation, and is applicable to unidirectional left or right shifts, bidirectional motion, or even complicated zigzag variations, and suitable for any amount of image shifts (whether less or more than one pixel).

III. IMAGE SENSOR DESIGN

A. Sensor Architecture

The block diagram of the proposed anti-vibration TDI CMOS image sensor is shown in Fig. 6. The sensor has six principal components. The first is a 4T-APS (4-transistor active pixel sensor) pixel array with 256×8 resolution, in which the 256 pixel columns define the spatial resolution of the image, and the 8 pixel rows facilitate the 8 TDI stages. The second component is 256 column-parallel TDI circuits, which execute the conventional TDI operation with optional ODB operation. The third component, the stage shifter, supplies the pixel control signals; the fourth component, a global pipeline output buffer, reads out the final photo signals after TDI operation, and the fifth and sixth components are a basic digital timing controller and an analog reference generator, respectively.

B. TDI Signal Path

Fig. 7 shows the whole signal path from pixel to output buffer. The 8 pixels in a given column, marked in yellow, act as the 8 TDI stages. The column-parallel TDI circuits are integrated with two blocks: a TDI accumulator (marked in

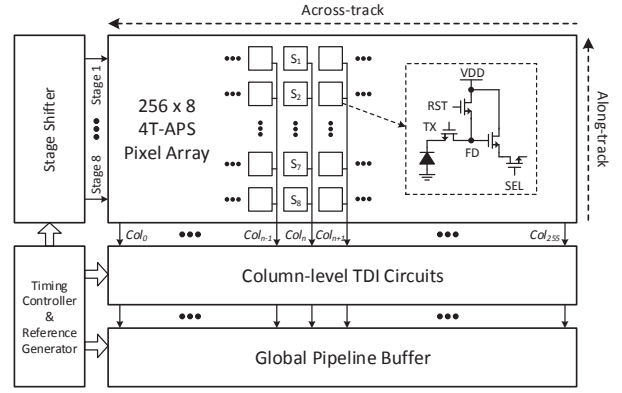


Fig. 6. Block diagram of the proposed anti-vibration TDI CMOS image sensor.

blue) and a single-stage memory (marked in red). The elements circled in green are the critical parasitic capacitances, which will be discussed in Section IV. Since the standard 4T-APS is applied here, reset noise cannot be neglected and the gain amplifier is therefore chosen as the basic structure, which also allows correlated double sampling (CDS) operations [28, 29]. The single-stage memory will read out the single-stage photo signal of each pixel with CDS operation, and the compensation capacitors ($C_{C1} \sim C_{C7}$), the different capacitance values of which implement the weight parameters (gain) in Eq. (6), will separately store the signals for subsequent neighbouring stage signal difference calculation. The TDI accumulator is designed to operate both conventional TDI accumulation and neighbouring stage difference accumulation. First, it reads out the single-stage photo signals with CDS and performs a conventional TDI accumulation with the C_{IA} as the input capacitor and one of the accumulation capacitors ($C_{A1} \sim C_{A8}$) as the feedback capacitor (which also stores the TDI accumulation signal). The TDI accumulator then calculates the photo signal difference and adds it to the same accumulation capacitor, with one of the compensation capacitors as the input capacitor and the same accumulation capacitor as feedback.

C. TDI Operation

Fig. 8 illustrates the simplified TDI timing diagram. After each integration, triggered by a global shutter, the stage shifter starts rolling in reverse order from *Stage8*. The TDI operation for each stage can be divided into two steps: the first step comprises conventional TDI accumulation and single-stage signal read out, and the second comprises neighbouring stage difference calculation and accumulation (available to *Stage8*~*Stage2*). In the first step in *Stage8*, the single-stage photo signal is added to the corresponding accumulation capacitor, and is also read out by the single-stage memory, but does not need to be stored because it is the last signal from a given object and there is no more subtraction. In the second step, the current signal is subtracted by the previous-time integration result stored in C_{C7} , and the difference is added to the same accumulation capacitor; it is then available to be read out to the output buffer. After *Stage8*, the stage shifter then turns to *Stage7*. In the first step, the single-stage photo signal is added to another corresponding accumulation capacitor, and

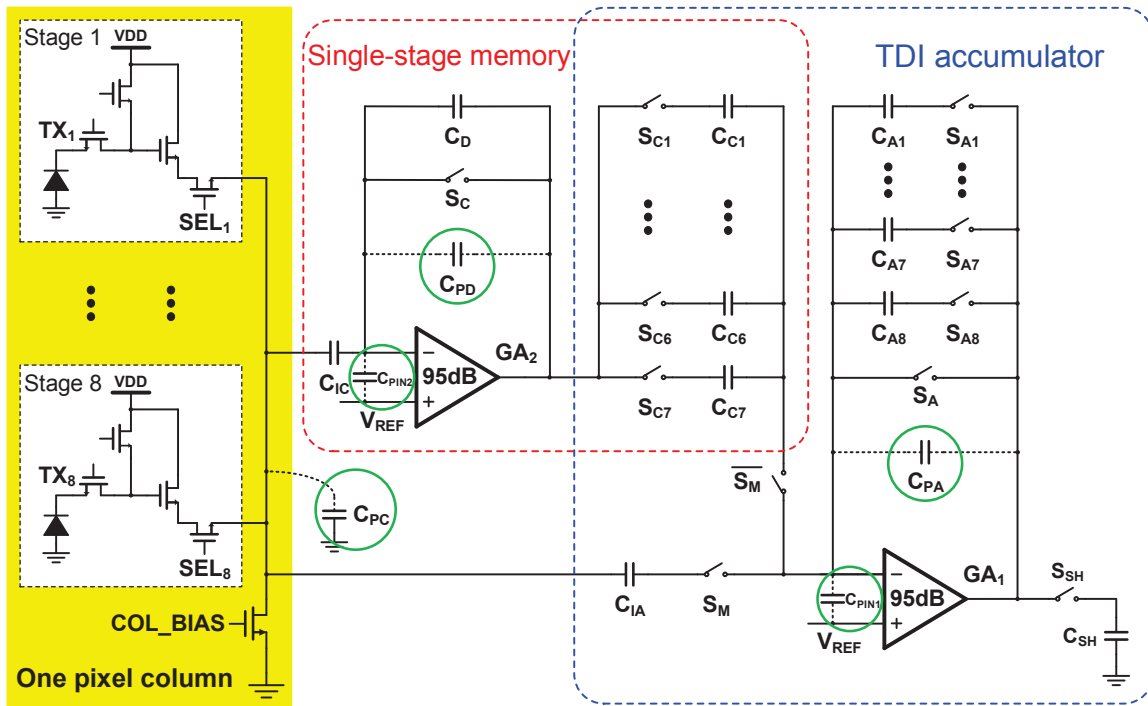


Fig. 7. The whole TDI signal path. The pixels are marked in yellow; the column-parallel TDI circuits, TDI accumulator and single-stage memory, are marked in blue and red respectively; and the parasitic capacitances are circled in green.

is also read out by the single-stage memory. Then a new difference between the *Stage7* photo signal and that stored in C_{C6} is produced and added to the same corresponding accumulation capacitor in the second step. Since C_{C7} is now free, it can be used to store the current *Stage7* photo signal for the neighboring stage signal difference calculation after the next integration. Following this reverse order, the same operations are carried out from *Stage6* to *Stage2*. In *Stage1*, where the neighboring stage signal difference is not available, only the first step is carried out. A new integration then begins.

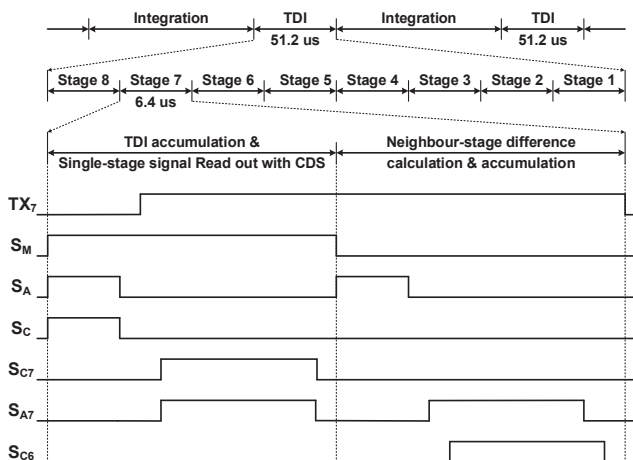


Fig. 8. The simplified TDI timing diagram.

In the TDI accumulator, the accumulation capacitors ($C_{A1} \sim C_{A8}$) are controlled by a TDI shifter, in line with the principle of storing photo signals produced from the same

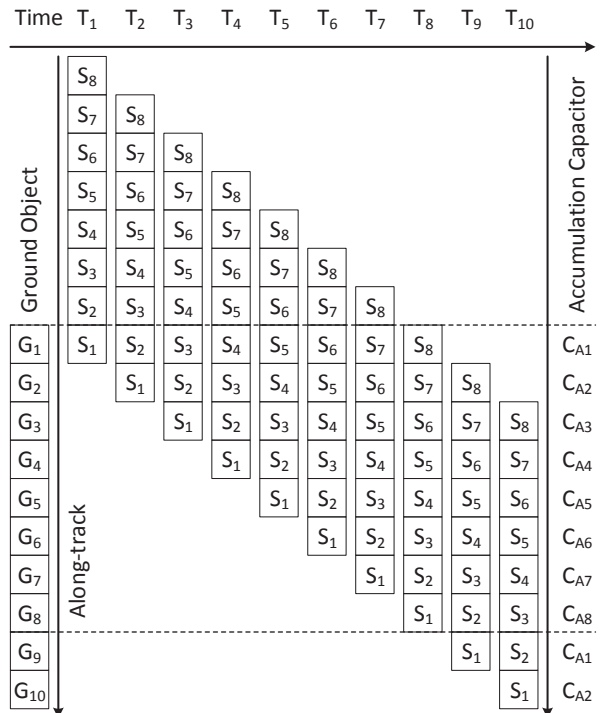


Fig. 9. TDI signal-to-capacitor arrangement rule.

object in the same capacitor. Fig. 9 describes the arrangement rule. $G_1 \sim G_{10}$ are the ground objects in the along-track direction to be imaged, $T_1 \sim T_{10}$ are the time instances when the pixel is performing integration, and $S_1 \sim S_8$ are pixels in one column. At T_1 , only S_1 is exposed to G_1 , the photo signal

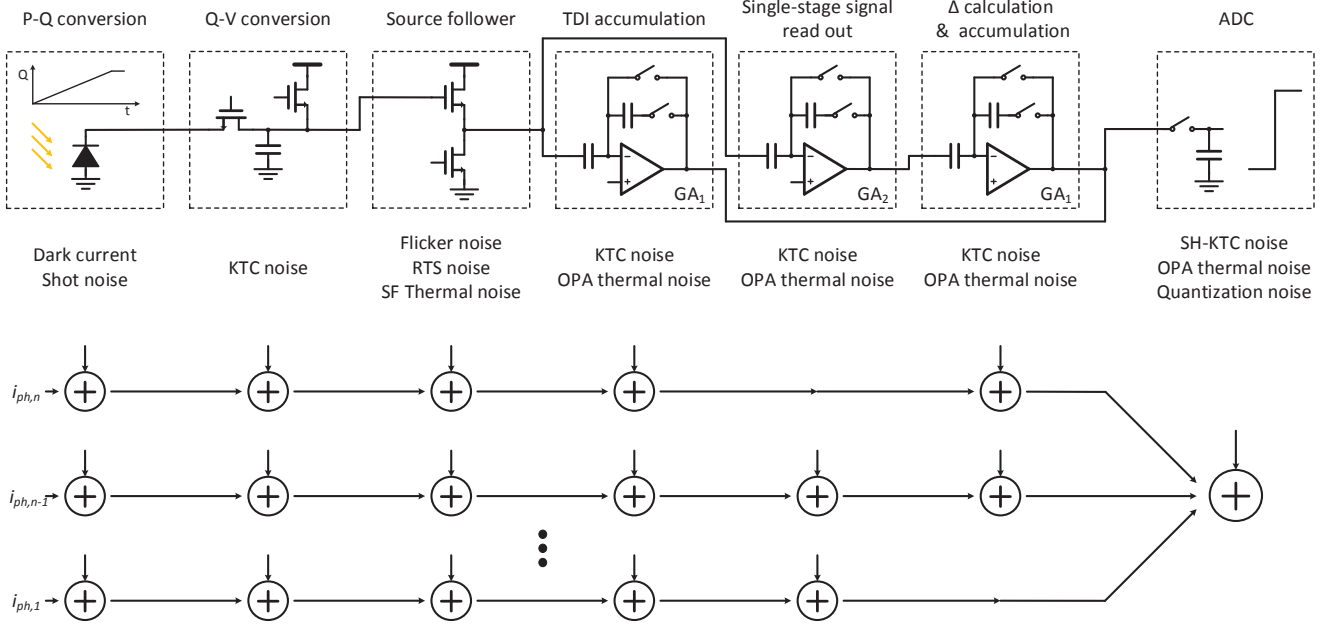


Fig. 10. Temporal noise model of the proposed TDI CMOS image sensor.

of which is output to C_{A1} . Then, at T_2 , after the sensor has advanced by one pixel, S_1 images G_2 and S_2 images G_1 , and the signals are stored in C_{A2} and C_{A1} , respectively. The same process is then repeated. Once a given ground object (G_1) has been projected to all the TDI stages, at T_8 in this case, C_{A1} collects the complete signal corresponding to G_1 . The signal is then read out and C_{A1} is reset, allowing the photo signal from a new ground object (G_9) to be stored in it at T_9 .

IV. NOISE ANALYSIS

In comparison with CCD, which can be considered noise-free during TDI operation, noise is a major challenge in the TDI CMOS image sensor. Time invariant noise, commonly known as fixed pattern noise (FPN), can be easily cancelled. This section therefore discusses temporal noise, such as shot noise, thermal noise and flicker noise, which may vary with the signal level and temperature [30–32]. Fig. 10 illustrates the temporal noise model for this anti-vibration TDI CMOS image sensor, from the photodiode to ADC. From Fig. 10, it can be seen that thermal noise is a predominant noise source during TDI operation, and increases the more TDI stages there are. Thermal noise is explained in detail in the next section.

A. Source Follower

In the source follower, the gate-to-source capacitor (C_{GS}) acts as a feedback, assuming the gain of the source follower is G_{SF} [31, 33]. In the TDI operation, the thermal noise of the source follower will be sampled in the capacitors in the TDI circuits, so the mean square noise voltage in the source follower output can be expressed as [34]

$$\overline{v_{SF}^2} \cong G_{SF}^2 \xi_{SF} \frac{k_B T}{g_{m,SF}} \omega \quad (8)$$

where, k_B is the Boltzmann constant, T is the absolute temperature, ξ_{SF} is the excess noise factor of the source follower, and $g_{m,SF}$ is the source follower transconductance. ω is the cut-off angular frequency, depending on the circuit configuration.

B. TDI Accumulator

In this design, all the TDI circuits are floor planned as column-parallel type circuits, with a long, narrow layout. Given such characteristics, the parasitic capacitance of the routing metal cannot be neglected. Five parasitic capacitances need to be taken into account: column bus parasitic capacitance C_{PC} , TDI accumulator feedback parasitic capacitance C_{PA} , single-stage memory feedback parasitic capacitance C_{PD} , and operational amplifier (OPA) input parasitic capacitances C_{PIN1} and C_{PIN2} , as shown in Fig. 7.

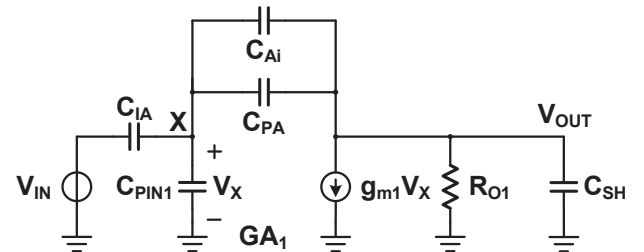


Fig. 11. Equivalent schematic diagram for TDI accumulator in the amplification phase of conventional TDI operation.

Fig. 11 shows the equivalent schematic diagram for the TDI accumulator in the amplification phase of a conventional TDI operation, where C_{Ai} is the accumulation capacitor ($i = 1, 2, \dots, 8$), and C_{IA} is the input capacitor. The gain of the TDI accumulator is thus given by

$$G_{1i} \cong \frac{C_{IA}}{C_{Ai} + C_{PA}} \quad (9)$$

Throughout the TDI operation, a given accumulation capacitor will sample the thermal noise of the source follower 8 times when reading out the pixel reset signal and 8 times when reading out the pixel photo signal. During the pixel reset signal read out, the thermal noise is sampled into the column bus parasitic capacitor C_{PC} and the input capacitors C_{IA} and C_{IC} , so the cut-off angular frequency is

$$\omega_{AR} \cong \frac{g_{m,SF}}{G_{SF}} \frac{1}{C_{IA} + C_{IC} + C_{PC}} \quad (10)$$

The noise is then transferred and sampled to the accumulation capacitor, and the mean square noise voltage is [33]

$$\overline{v_{SF,ARi}^2} \cong G_{1i}^2 G_{SF} \xi_{SF} \frac{k_B T}{C_{IA} + C_{IC} + C_{PC}} \quad (11)$$

During the reading out of the pixel photo signal, thermal noise will be directly sampled into the accumulation capacitor after being amplified by GA_1 . In this case, the cut-off angular frequency is

$$\omega_{AOi} \cong \frac{g_{m1} C_{Ai}'}{C_{SH} C_{IN1}' + C_{SH} C_{Ai}' + C_{IN1}' C_{Ai}'} \quad (12)$$

where $C_{IN1}' = C_{IA} + C_{PIN1}$, $C_{Ai}' = C_{Ai} + C_{PA}$, g_{m1} is the transconductance of the operational amplifier in GA_1 , and the mean square noise voltage is given by

$$\overline{v_{SF,AOi}^2} \cong G_{1i}^2 G_{SF}^2 \xi_{SF} \frac{k_B T}{g_{m,SF}} \omega_{AOi} \quad (13)$$

Another source of thermal noise during amplification is the operational amplifier. This contribution is also sampled, and is given by

$$\overline{v_{OPA,Ai}^2} \cong \left(1 + \frac{C_{IN1}'}{C_{Ai}'}\right)^2 \xi_1 \frac{k_B T}{g_{m1}} \omega_{AOi} \quad (14)$$

where ξ_1 is the excess noise factor of the operational amplifier, including the noise of all the internal transistors. The input-referred noise (or floating diffusion (FD) referred noise) caused by the TDI accumulator in the conventional TDI phase can therefore be expressed as

$$\overline{v_{A,total}^2} \cong 8 \left(\frac{\overline{v_{SF,ARi}^2} + \overline{v_{SF,AOi}^2} + \overline{v_{OPA,Ai}^2}}{G_{SF}^2 G_{1i}^2} \right) \quad (15)$$

C. Single-Stage Memory

Synchronized by the TDI accumulation, the single-stage memory will read out the signal-stage photo signal. The operation is similar to that of the TDI accumulator, the only differences being that the signal is read out only once, and then stored in a compensation capacitor rather than 8 times in the feedback capacitor. The equivalent schematic diagram for this phase is shown in Fig. 12, where C_{IC} , C_D and C_{Cj} ($j = 1, 2, \dots, 7$) are the input capacitor, feedback capacitor and load capacitor, respectively. And the gain of GA_2 is

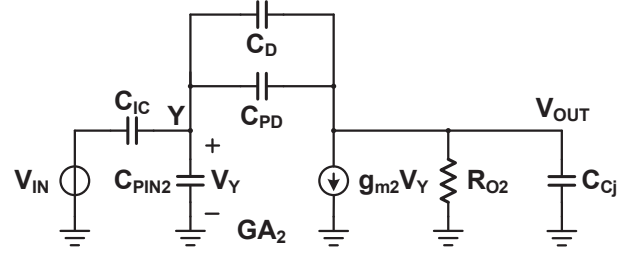


Fig. 12. Equivalent schematic diagram for single-stage memory in the photo signal read out phase.

$$G_2 \cong \frac{C_{IC}}{C_D + C_{PD}} \quad (16)$$

The mean square thermal noise voltages generated by the source follower during the pixel reset signal can be expressed as [33]

$$\overline{v_{SF,DR}^2} \cong G_2^2 G_{SF} \xi_{SF} \frac{k_B T}{C_{IA} + C_{IC} + C_{PC}} \quad (17)$$

The mean square thermal noise voltages generated by the source follower during the pixel photo signal are given as

$$\overline{v_{SF,DOj}^2} \cong G_2^2 G_{SF}^2 \xi_{SF} \frac{k_B T}{g_{m,SF}} \omega_{DOj} \quad (18)$$

Assuming that $C_{IN2}' = C_{IC} + C_{PIN2}$, $C_{D}' = C_D + C_{PD}$, and the transconductance of the operational amplifier in GA_2 is g_{m2} , then the cut-off angular frequency can be written as

$$\omega_{DOj} \cong \frac{g_{m2} C_{D}'}{C_{Cj} C_{IN2}' + C_{Cj} C_{D}' + C_{IN2}' C_{D}'} \quad (19)$$

The mean square thermal noise voltage contributed by the operational amplifier in GA_2 is

$$\overline{v_{OPA,Dj}^2} \cong \left(1 + \frac{C_{IN2}'}{C_{D}'}\right)^2 \xi_2 \frac{k_B T}{g_{m2}} \omega_{DOj} \quad (20)$$

where ξ_2 is the excess noise factor including the noise of all the internal transistors inside the operational amplifier.

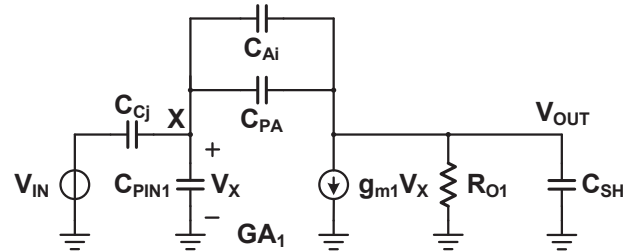


Fig. 13. Equivalent schematic diagram for TDI accumulator in the compensation phase.

After the single-stage signal read out, the neighbouring stage signal difference is calculated and accumulated to the accumulation capacitors. Fig. 13 shows the equivalent schematic diagram for the TDI accumulator in this phase, in which three

types of noise are introduced. The first noise source is the source follower, the thermal noise of which is amplified by the gain amplifiers in both the single-stage memory (GA_2) and the TDI accumulator (GA_1). The mean square noise voltage is thus given by

$$\overline{v_{SF,DAj}^2} \cong G_{DAj}^2 G_2^2 G_{SF}^2 \xi_{SF} \frac{k_B T}{g_{m,SF}} \omega_{DAj} \quad (21)$$

where G_{DAj} is the weight parameters in Eq. (6), and can be defined as

$$G_{DAj} \cong \frac{C_{Cj}}{C_{Ai} + C_{PA}} \quad (22)$$

And the cut-off angular frequency is

$$\omega_{DAj} \cong \frac{g_{m1} C_{Ai}'}{(C_{SH} + C_{Ai}') (C_{Cj} + C_{PIN1}) + C_{SH} C_{Ai}'} \quad (23)$$

The second noise source is the operational amplifier in GA_2 . Its noise will be amplified by the GA_1 , then sampled into an accumulation capacitor. Here, the mean square noise voltage is given by

$$\overline{v_{OPA,DAj}^2} \cong G_{DAj}^2 \left(1 + \frac{C_{IN2}'}{C_D'}\right)^2 \xi_2 \frac{k_B T}{g_{m2}} \omega_{DAj} \quad (24)$$

The last noise source is the operational amplifier in GA_1 . The mean square noise voltage is given by

$$\overline{v_{OPA,ADj}^2} \cong \left(1 + \frac{C_{Cj} + C_{PIN1}}{C_{Ai}'}\right)^2 \xi_1 \frac{k_B T}{g_{m1}} \omega_{DAj} \quad (25)$$

Considering the circuit operation, the noise generated during the pixel reset signal read out, shown in Eq. (17), can be partially removed during neighbouring stage difference accumulation, as in the CDS operation, and the total input-referred thermal noise in a given accumulation capacitor can be expressed as

$$\begin{aligned} \overline{v_{D,total}^2} \cong & \sum_{j=1}^7 \frac{\overline{v_{SF,DAj}^2} + \overline{v_{OPA,DAj}^2} + \overline{v_{OPA,ADj}^2}}{G_{SF}^2 G_{1i}^2} \\ & + \sum_{j=1}^7 \frac{G_{DAj}^2 (\overline{v_{SF,DOj}^2} + \overline{v_{OPA,Dj}^2})}{G_{SF}^2 G_{1i}^2} \\ & + 8 \left(\frac{\overline{v_{SF,DR}^2}}{G_{SF}^2 G_{1i}^2} \right) \end{aligned} \quad (26)$$

According to the analysis detailed above, $\overline{v_{A,total}^2}$ is the thermal noise introduced by the conventional TDI operation, and $\overline{v_{D,total}^2}$ is the thermal noise caused by the ODB algorithm. From Section III-C, it can be seen that the conventional TDI scheme only has one operation after each integration, while, the ODB algorithm carries out two extra operations. Since the operations are executed by the gain amplifiers, the noise of one extra operation (adding neighbouring stage signal difference to accumulation capacitor) could be removed. And the total thermal noise of the ODB algorithm is about twice of that of the conventional TDI scheme. These can also be

verified in Eq. (15) and Eq. (26). Therefore applying the ODB algorithm would increase the noise level and decrease the dynamic range and the signal-to-noise ratio. With the number of TDI stage increases, the gain expressed in Eq. (6) grows, so the corresponding noise expressed in Eq. (25) increases. This would limit the number of TDI stages using the ODB algorithm.

V. SENSOR IMPLEMENTATION AND MEASUREMENT RESULT

A prototype 256×8-pixel chip was implemented using a 0.18 μm CMOS image sensor process (1P6M). Since many capacitors are employed per column circuit, one column would inevitably occupy a long stripe area in physical implementation. For the sake of improved column-wise matching, the two gain amplifiers GA_1 and GA_2 , with their associated capacitors (see Fig. 7) were placed on the top and bottom sides of the pixel array, respectively. Fig. 14 shows a microphotograph of the prototype chip.

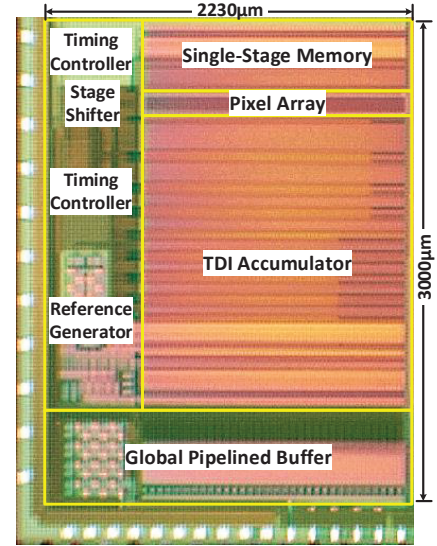


Fig. 14. Microphotograph of the proposed anti-vibration TDI CMOS image sensor.

Fig. 15 illustrates the vibration test platform. The whole platform is placed on an optical table in a dark room. The proposed TDI CMOS image sensor is mounted on a motor-based vibration generator, capable of making the sensor vibrate in the across-track direction with tuneable frequency and amplitude. The vibration generator was fixed to a linear motor that provided uniform motion for the camera movement. During operation, the TDI sensor moves in the along-track direction at a constant speed and zigzag vibrates in the across-track direction. The target is scanned during the sensor movement, and the images produced are collected by the computer.

Fig. 16 shows a sample image taken by the proposed 8-stage TDI image sensor in conventional mode, and Fig. 17 shows sample TDI images with and without vibration in the across-track direction. In accordance with the problem statement in Section II-A, two mid-range vibration frequencies (50Hz and 100Hz), and two image shifts (1/2 pixel and 1/4 pixel)

TABLE I
PERFORMANCE SUMMARY AND COMPARISON

Parameters	This work		Ref.[3]	Ref.[4]	Ref.[6]
	w/o ODB	w/ ODB			
Technology	0.18 μ m CIS 1P6M		0.18 μ m CMOS 1P4M	0.35 μ m CMOS	0.18 μ m CIS 1P6M
TDI Architecture	TDI accumulator with ODB		TDI accumulator	TDI accumulator	Adjacent pixel transfer
Pixel Type	4T-APS		4T-APS	3T-APS	4T-APS
Resolution	256 \times 8		128 \times 32	8000 \times 25	128 \times 8 \times 2
Pixel Size	6.5 \times 6.5 μ m ²		15 \times 15 μ m ²	13 \times 13 μ m ²	6 \times 6 μ m ²
Fill Factor	28 %		67 %	48 %	26.99 %
Max. Line Rate	1.74 kHz		3.875 kHz	-	1.6 kfps
Max. Data Rate	40 MHz		-	-	-
Sensitivity ¹	14769 e-/lux·s (1.79 V/lux·s)		3.2 V/lux·s	-	2 V/lux·s
Dark Current	54.9 e-/s (6.65 mV/s)		-	-	-
FPN	0.45 % (9.0 mV)	1.82 % (36.4 mV)	2.1~3.1 mV	24~60 mV	-
Input-Referred Noise	42.4 e-	91.6 e-	-	-	-
SNR Boost to 1 Stage	8.6 dB	1.9 dB	11.9~14.2 dB	-	9.56~10.33 dB
DR	51.8 dB	45.1 dB	40.5~44.8 dB	-	-
Energy Consumption	0.46 μ J/pixel		0.22 μ J/pixel	-	0.0026 μ J/pixel

¹ The numbers listed in this row are the sensitivities for single stage.

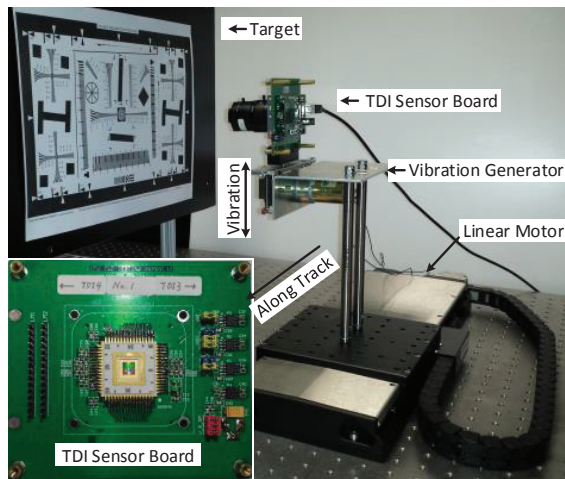


Fig. 15. Vibration test platform for the proposed anti-vibration TDI CMOS image sensor.



Fig. 16. Sample TDI image taken by the proposed sensor in conventional mode without vibration.

were used. The image without vibration seemed to have the best image quality ($ASF = 297$). When subject to vibration, the images manifested different levels of degradation. The images without the ODB algorithm (Fig. 17(c)(e)(g)) had the worst image quality: the corners and edges were blurred, and some small details, like the dash in the “f”, were lost. In contrast, the images produced using the ODB algorithm (Fig. 17(b)(d)(f)), despite displaying geometric distortion in the across-track direction, had clear corners, sharp edges and better image quality. With the same vibration frequency, larger vibration level led to worse sharpness. In the conventional TDI scheme (Fig. 17(c)(e)), larger vibration made the image shifts of each TDI stage bigger, producing a blurred output image (Fig. 17(e)). In the ODB solution (Fig. 17(b)(d)), however, larger vibration levels led to wider geometric distortion, with the associated lower gradient: this explains why the ASF value of Fig. 17(d) is lower than that of Fig. 17(b). Similarly, with the same vibration level, higher vibration frequency leads to more blur, because a higher vibration frequency in a given field of view (FOV) results in a larger image shift in each TDI stage. Thus, in the conventional TDI scheme, Fig. 17(g) is more blurred than Fig. 17(e), whereas with the ODB algorithm, the ASF value of Fig. 17(f) is lower than that of Fig. 17(d). In conclusion, with vibration the conventional TDI scheme produces blurry images and lacks details, whereas the ODB algorithm, despite containing geometric distortion, can capture all the details and obtain sharp images without the help of any other devices or equipment.

Table I summarizes the benchmark results of the prototype image sensor against a few recently reported TDI CMOS image sensors. Despite the main merits of this work that can correct the blurred image, the noise performance is not as good as the prior works. We believe that this is mainly due to the complexity of the algorithm, which involves many stages of



Fig. 17. Sample TDI images without vibration and with vibration (including variable levels and frequencies).

signal amplification and addition, sample and hold, and each of which was polluted by noise. The physical implementation of the analog path results in a silicon area of $2265\mu\text{m} \times 6.5\mu\text{m}$ per column. The parasitic capacitance associated with the long metal bus brings in a lot of variations, which degrades its permanence in terms of FPN as well as noise. Leakage currents, including channel leakage of the switch transistors (e.g., S_{A1} , S_{A2} , ..., S_{A8}) and the leakage of the capacitors themselves, also cause loss to the stored signals. Finally, it can be noticed that this design has a higher energy dissipation ($0.46\mu\text{J}/\text{pixel}$). Ref.[6] is based on adjacent pixel signal transfer scheme, the internal buffer of the signal path only needs to be enabled for a short period by the end of each exposure stage, while in this work and Ref.[3], the gain amplifiers need to be kept working all the time, thus the energy dissipation is much higher.

VI. CONCLUSION

Vibrations in the flight path can easily cause conventional TDI image sensors to lose details and produce only blurry images. To solve this problem, this paper proposes a new TDI CMOS image sensor based on an ODB algorithm. Superior to conventional TDI image sensors, the proposed sensor can prevent photo signals from becoming mixed up due to vibrations, making it possible to capture details and generate sharp TDI images without the help of additional devices or equipment. The proposed method opens a door that will facilitate the design of remote imaging systems by alleviating most of the design constraints associated with pointing accuracy, vibration modelling and cancellation. The sensor is suitable for small remote imaging systems, e.g., nano-satellites and pico-satellites. Future work is suggested to improve the noise performance of the existing signal path: the parasitic capacitances could be

decreased by doubling the pitch of the signal path, and placing the circuits for odd columns below the pixel array and those for even columns above the pixel array. Leakage current could be reduced by using negative voltage control signals. Further innovation in sensor architecture can be expected to achieve higher signal-to-noise ratio and dynamic range.

VII. ACKNOWLEDGEMENT

This work was supported by S13-1109-NRFOSTIn-SRP and RG 100/14 (2014-T1-001-105).

REFERENCES

- [1] G. Lepage, J. Bogaerts, and G. Meynants, "Time-Delay-Integration Architectures in CMOS Image Sensors," *IEEE Trans. on Electron Devices*, vol. 56, no. 11, pp. 2524–2533, Nov. 2009.
- [2] K. Nie, S. Yao, J. Xu, J. Gao, and Y. Xia, "A 128-Stage Analog Accumulator for CMOS TDI Image Sensor," *IEEE Trans. on Circuits and Systems I: Regular Papers*, vol. 61, no. 7, pp. 1952–1961, Jul. 2014.
- [3] K. Nie, S. Yao, J. Xu, and J. Gao, "Thirty Two-Stage CMOS TDI Image Sensor With On-Chip Analog Accumulator," *IEEE Trans. on Very Large Scale Integration (VLSI) Systems*, vol. 22, no. 4, pp. 951–956, Apr. 2014.
- [4] G. Lepage, D. Dants, and W. Diels, "CMOS Long Linear Array for Space Application," *Proc. SPIE*, vol. 6068, pp. 606 807–606 807–8, Feb. 2006.
- [5] H. Yu, X. Qian, S. Chen, and K.-S. Low, "A Time-Delay-Integration CMOS Image Sensor with Pipelined Charge Transfer Architecture," in *IEEE International Symposium on Circuits and Systems (ISCAS)*, May 2012, pp. 1624–1627.

- [6] J.-H. Chang, K.-W. Cheng, C.-C. Hsieh, W.-H. Chang, H.-H. Tsai, and C.-F. Chiu, "Linear CMOS Image Sensor with Time-Delay Integration and Interlaced Super-resolution Pixel," in *IEEE Sensors*, Oct. 2012, pp. 1–4.
- [7] K.-W. Cheng, C. Yin, C.-C. Hsieh, W.-H. Chang, H.-H. Tsai, and C.-F. Chiu, "Time-Delay Integration Readout with Adjacent Pixel Signal Transfer for CMOS Image Sensor," in *International Symposium on VLSI Design, Automation, and Test (VLSI-DAT)*, Apr. 2012, pp. 1–4.
- [8] X. He and O. Nixon, "Time Delay Integration Speeds Up Imaging," *Photonics Spectra*, vol. 46, no. 5, pp. 50–54, May 2012.
- [9] D. X. D. Yang and A. El Gamal, "Comparative Analysis of SNR for Image Sensors with Enhanced Dynamic Range," *Proc. SPIE*, vol. 3649, pp. 197–211, Apr. 1999.
- [10] A. Lustica, "CCD and CMOS Image Sensors in New HD Cameras," in *Proc. on ELMAR*, Sept. 2011, pp. 133–136.
- [11] A. Theuwissen, "CCD or CMOS Image Sensors for Consumer Digital Still Photography?" in *International Symposium on VLSI Technology, Systems, and Applications (VLSI-TSA)*, Apr. 2001, pp. 168–171.
- [12] P. Centen, *CCD Imaging: Concepts for Low Noise and High Bandwidth*. Technische Universiteit Eindhoven, 1999.
- [13] W. L. Hayden, T. McCullough, A. Reth, and D. M. Kaufman, "Wideband Precision Two-Axis Beam Steerer Tracking Servo Design and Test Results," *Proc. SPIE*, vol. 1866, pp. 271–279, Aug. 1993.
- [14] M. E. Wittig, L. van Holtz, D. E. L. Tunbridge, and H. C. Vermeulen, "In-Orbit Measurements of Microaccelerations of ESA's Communication Satellite Olympus," *Proc. SPIE*, vol. 1218, pp. 205–214, Jul. 1990.
- [15] O. Hadar, M. Fisher, and N. S. Kopeika, "Image Resolution Limits Resulting from Mechanical Vibrations. Part III: Numerical Calculation of Modulation Transfer Function," *Optical Engineering*, vol. 31, no. 3, pp. 581–589, Mar. 1992.
- [16] A. Tan, T. Meurers, S. Veres, G. Aglietti, and E. Rogers, "Satellite Vibration Control Using Frequency Selective Feedback," in *IEEE Conference on Decision and Control*, vol. 2, Dec. 2003, pp. 1693–1698.
- [17] G. S. Aglietti, R. S. Langley, E. Rogers, and S. B. Gabriel, "An Efficient Model of an Equipment Loaded Panel for Active Control Design Studies," *Acoustical Society of America*, vol. 108, no. 4, pp. 1663–1673, Oct. 2000.
- [18] S. Hemmati, M. Shahravi, and K. Malekzadeh, "Active Vibration Control of Satellite Flexible Structures during Attitude Maneuvers," *Research Journal of Applied Sciences, Engineering and Technology*, vol. 5, no. 15, pp. 4029–4037, 2013.
- [19] Z. Zheng, J. Wu, H. Feng, Z. Xu, Q. Li, and Y. Chen, "Image Restoration of Hybrid Time Delay and Integration Camera System with Residual Motion," *Optical Engineering*, vol. 50, no. 6, pp. 067 012–067 012–10, Jun. 2011.
- [20] Y. Xu, X. Hu, and S. Peng, "Robust Image Deblurring Using Hyper Laplacian Model," in *Computer Vision - ACCV 2012 Workshops*, ser. Lecture Notes in Computer Science. Springer Berlin Heidelberg, 2013, vol. 7729, pp. 49–60.
- [21] S. Nayar and M. Ben-Ezra, "Motion-Based Motion Deblurring," *IEEE Trans. on Pattern Analysis and Machine Intelligence*, vol. 26, no. 6, pp. 689–698, Jun. 2004.
- [22] W. H. Richardson, "Bayesian-Based Iterative Method of Image Restoration," *Journal of the Optical Society of America*, vol. 62, no. 1, pp. 55–59, Jan. 1972.
- [23] L. B. Lucy, "An Iterative Technique for the Rectification of Observed Distributions," *The Astronomical Journal*, vol. 79, no. 6, pp. 745–755, Jun. 1974.
- [24] C. Wang, L. Sun, Z. Chen, J. Zhang, and S. Yang, "Multi-Scale Blind Motion Deblurring Using Local Minimum," *Inverse Problems*, vol. 26, no. 1, p. 015003, Jan. 2010.
- [25] T. Michaeli and M. Irani, "Blind Deblurring Using Internal Patch Recurrence," in *Computer Vision ECCV 2014*, ser. Lecture Notes in Computer Science. Springer International Publishing, 2014, vol. 8691, pp. 783–798.
- [26] F. Kerouh and A. Serir, "Wavelet-Based Blind Blur Reduction," *Signal, Image and Video Processing*, pp. 1–13, Jan. 2014.
- [27] N. Kehtarnavaz and H.-J. Oh, "Development and Real-time Implementation of a Rule-based Auto-focus Algorithm," *Real-Time Imaging*, vol. 9, no. 3, pp. 197–203, Jun. 2003.
- [28] J. Ohta, *Smart CMOS Image Sensors and Applications*. CRC Press, 2007.
- [29] Y. Chen, Y. Xu, Y. Chae, A. Mierop, X. Wang, and A. Theuwissen, "A 0.7e-rms-Temporal-Readout-Noise CMOS Image Sensor for Low-light-level Imaging," in *IEEE International Solid-State Circuits Conference (ISSCC)*, Feb. 2012, pp. 384–386.
- [30] H. Wach and E. R. Dowski, Jr., "Noise Modeling for Design and Simulation of Computational Imaging Systems," *Proc. SPIE*, vol. 5438, pp. 159–170, Jul. 2004.
- [31] R. Gow, D. Renshaw, K. Findlater, L. Grant, S. McLeod, J. Hart, and R. Nicol, "A Comprehensive Tool for Modeling CMOS Image-Sensor-Noise Performance," *IEEE Trans. on Electron Devices*, vol. 54, no. 6, pp. 1321–1329, Jun. 2007.
- [32] P. Martin-Gonthier and P. Magnan, "RTS Noise Impact in CMOS Image Sensors Readout Circuit," in *IEEE International Conference on Electronics, Circuits, and Systems (ICECS)*, Dec. 2009, pp. 928–931.
- [33] S. Kawahito, "Signal Processing Architectures for Low-Noise High-Resolution CMOS Image Sensors," in *IEEE Custom Integrated Circuits Conference (CICC)*, Sept. 2007, pp. 695–702.
- [34] Y. Chen, Y. Xu, A. Mierop, and A. J. P. Theuwissen, "Column-Parallel Digital Correlated Multiple Sampling for Low-Noise CMOS Image Sensors," *IEEE Sensors Journal*, vol. 12, no. 4, pp. 793–799, Apr. 2012.